Characterization of tandem aerosol classifiers for selecting particles: implication for eliminating multiple charging effect

Yao Song[1], Xiangyu Pei[1], Huichao Liu[1], Jiajia Zhou[1], Zhibin Wang[1,2,3*]

[1] College of Environmental and Resource Sciences, Zhejiang Provincial Key Laboratory of Organic Pollution Process and Control, Zhejiang University, Hangzhou, 310058, China
[2]Hangzhou Global Scientific and Technological Innovation Center, Zhejiang University, Hangzhou, 311200, China
[3]Key Laboratory of Environment Remediation and Ecological Health, Ministry of Education, Zhejiang University, 310058 Hangzhou, China

Correspondence to: Zhibin Wang (wangzhibin@zju.edu.cn)

Abstract. Accurate particle classification plays a vital role in aerosol studies. Differential mobility analyzer (DMA), centrifugal particle mass analyzer (CPMA) and aerodynamic aerosol classifier (AAC) are commonly used to select particles with a specific size or mass. However, multiple charging effects cannot be entirely avoided when using either individual techniques or tandem systems such as DMA-CPMA, especially when selecting soot particles with fractal structures. In this study, we demonstrate the transfer functions of the DMA-CPMA and DMA-AAC in static configurations. We propose an equation that constrains the resolutions of DMA and CPMA to eliminate the multiple charging effect when selecting particles with a certain mass–mobility relationship using the DMA-CPMA system. The equation for the DMA-AAC system is also derived. Our results show that the ability to remove multiply charged particles mainly depends on the particle morphology and resolutions of the DMA and CPMA. Using measurements from soot experiments and literature data, a general trend in the appearance of multiple charging effect with decreasing size when selecting aspherical particles is observed. Otherwise, our results indicate that the ability of the DMA-AAC in a static configuration to eliminate particles with multiple charges is mainly related to the resolutions of classifiers. In most cases, the DMA-AAC in a static configuration can eliminate multiple charging effect regardless of the particle morphology, but multiply charged particles will be selected when decreasing the resolution of the DMA or AAC. We propose that the potential influence of the multiple charging effect should be considered when using the DMA-CPMA or DMA-AAC systems in estimating size- and mass-resolved optical properties in field and lab experiments.

1 Introduction

Atmospheric aerosol particles span a wide size range from 1 nm to > 100 μm. A significant size dependence of aerosol physicochemical properties has been widely reported. Particle size can strongly alter the hygroscopic behavior (Biskos et al., 2006), phase state (Cheng et al., 2015) and cloud-nucleating ability

(Dusek et al., 2006) of aerosol nanoparticles, indicating the importance of particle size when assessing the climate effect. Hence, accurate particle classification is essential when investigating the size dependence behavior of aerosol particles.

At present, particles are generally classified by either size or mass in atmospheric aerosol studies. A differential mobility analyzer (DMA) is the most commonly used size classifier, which selects particles based on electrical mobility (Knutson and Whitby, 1975; Park et al., 2008; Stolzenburg and McMurry, 2008; Swietlicki et al., 2008; Wiedensohler et al., 2012). A particle mass analyzer (PMA) includes an aerosol particle mass analyzer (APM) and a centrifugal particle mass analyzer (CPMA), both of which classify particles based on their mass-to-charge ratio (Ehara et al., 1996; Olfert and Collings, 2005). However, particles must be precharged when classified by a DMA or PMA because DMA and PMA classify particles based on electrical mobility and mass-to-charge ratio, resulting in particles with higher-order charges and identical apparent mobility or mass-to-charge ratio being selected simultaneously, which are referred to as the multiple charging effect. This may introduce uncertainty in the subsequent characterization. Radney et al. (2013) demonstrated that although single-charged particles account for the highest number fraction (46.3%) of DMA-classified particles (200 nm), their contributions to the total mass concentration and extinction are insignificant (10.8% and 7.96%, respectively). Thus, the reported extinction of particles with a certain diameter has been greatly overestimated due to the multiple charging effect.

Previous studies (Shiraiwa et al., 2010;Rissler et al., 2013; Johnson et al., 2014; Johnson et al., 2021) tried to utilize the combination of size and mass classifiers, such as DMA-APM or DMA-CPMA systems, to obtain singly charged particles. Theoretically, the ability of a DMA-APM to eliminate multiply charged particles is governed by the particle morphology and setups of DMA-APM (Kuwata, 2015). This conclusion implies that multiply charged particles cannot be effectively excluded for aspherical particles, especially for soot particles. Radney and Zangmeister (2016) investigated the limitations of a DMA-APM with three types of particles (polystyrene latex (PSL) spheres, ammonium sulfate (AS) and soot particles). Their results demonstrated that a DMA-APM can resolve multiply charged particles for spherical particles (PSL and AS particles), but it failed for aspherical soot particles. Multiply charged soot particles led to over 110% errors in retrieving the mass specific extinction cross section.

In contrast to DMA and PMA, an aerodynamic aerosol classifier (AAC) is a novel instrument that selects the aerodynamic equivalent diameter of aerosol particles based on their relaxation time. The advantage of utilizing an AAC is that no charging process is needed in particle classification compared with the aforementioned classifiers; hence, multiple charging effects can be avoided (Tavakoli and Olfert, 2013). However, the selected particles are not monodispersed in mobility diameter when an AAC is used to select aspherical particles (Kazemimanesh et al., 2022).

Morphology information, such as effective density (ρ_{eff}), mass–mobility exponent (D_{fm}) and dynamic shape factor (χ), can be inferred using tandem DMA-PMA system (Park et al., 2003; Zhang et al., 2008; Rissler et al., 2013; Pei et al., 2018; Zangmeister et al., 2018), DMA-AAC (Tavakoli and Olfert, 2014) and AAC-CPMA systems (Johnson et al., 2018). The derived ρ_{eff} and χ depend upon the combination of instruments used, while the nonphysical values of χ and ρ_{eff} for aspherical particles can be determined by the AAC-APM(Yao et al., 2020) and AAC-CPMA (Kazemimanesh et al., 2022).

The theoretical transfer functions of individual classifiers (DMA, CPMA and AAC) and the DMA-APM system have been previously discussed (Knutson and Whitby, 1975; Ehara et al., 1996; Olfert and Collings, 2005; Stolzenburg and McMurry, 2008; Tavakoli and Olfert, 2013). In this study, we focus on a DMA-CPMA and DMA-AAC in static configurations to eliminate multiply charged particles. The DMA-CPMA and DMA-AAC systems mentioned below refer to the tandems of a DMA and CPMA or a DMA and AAC in a static configuration, respectively. We calculate the transfer functions of the DMA-AAC and DMA-CPMA systematically. Combined with soot experiments, we demonstrate that multiple charging effects may still exist after DMA-CPMA classification when selecting aspherical particles and evaluate the light absorption of selected particles with different charging states using Mie theory. Furthermore, we propose operating conditions for the DMA-CPMA and DMA-AAC to eliminate multiply charged particles in future studies. Our results suggest that the size- and mass-resolved optical properties may be overestimated for small soot particles when using the DMA-CPMA system, which will lower the prediction accuracy of the fresh soot climate effect. In Sect. 3.1, we calculate the transfer functions of the DMA-CPMA and DMA-AAC utilizing the literature data of soot particles from Pei et al. (2018). In Sect. 3.2, we measure the multiple charging effect of the DMA-CPMA using laboratory-generated soot particles, and the bias of optical measurement induced by multiply charged particles is evaluated in Sect. 3.3.

2 Theory and experiment

2.1 Transfer function for individual aerosol classifiers

DMA

The DMA, consisting of two coaxial electrodes, classifies particles based upon electrical mobility Z_{p} (Knutson and Whitby, 1975), which can be calculated as follows:

$$Z_p = q\mathrm{B} = \frac{neCc(d_m)}{3\pi\mu d_m}, \tag{1}$$

where q is the particle charge, n is the number of elementary charges, B is the mobility of the particle, e is the elemental charge, μ is the viscosity of air, and $Cc(d_{\mathrm{p}})$ is the Cunningham slip correction factor. When the aerosol inlet flow rate equals the aerosol sampling outlet flow rate, the Z_{p}* selected by the DMA is defined as

$$Z_p^* = \frac{Q_{sh}}{2\pi V_{DMA} L_{DMA}} \ln\left(\frac{r_{2\_DMA}}{r_{1\_DMA}}\right), \tag{2}$$

where Q_{sh} is the sheath flow rate, V_{DMA} is the voltage between the two electrodes, L_{DMA} is the length of the DMA, and r_{1_DMA} and r_{2_DMA} are the inner and outer radii of the DMA, respectively. Assuming that the aerosol inlet and aerosol sampling flow rates are equal, the transfer function of the DMA can be expressed as follows when particle diffusion is negligible (Knutson and Whitby, 1975; Stolzenburg and McMurry, 2008):

$$\Omega(\tilde{Z}_p, \beta_{DMA}) = \frac{1}{2\beta_{DMA}}\left[\left|\tilde{Z}_p - (1+\beta_{DMA})\right| + \left|\tilde{Z}_p - (1-\beta_{DMA})\right| - 2\left|\tilde{Z}_p - 1\right|\right] , \tag{3}$$

where, $\tilde{Z}_p = Z_p/Z_p^*$, $\beta_{\mathrm{DMA}}=Q_a/Q_{sh}$, and Q_a is the sample flow rate. The limiting electrical mobilities that DMA can select are $(1 \pm \beta_{\mathrm{DMA}})\cdot Z_p^*$. The maximum and minimum values of d_m for particles with n charges can be derived and denote as $d_{m\ n,max}$ and $d_{m\ n,min}$, respectively. The transfer function is an isosceles triangle with value of 1 at Z_p^* and going to 0 at $(1 \pm \beta_{\mathrm{DMA}})\cdot Z_p^*$. It translates to asymmetry in d_m since the relationship between d_m and Z_p is nonlinear.

CPMA

The construction of the CPMA is similar to the APM, but its inner cylinder rotates faster than the outer cylinder to create a stable system of forces (Olfert and Collings, 2005). In the CPMA, the equation of particle motion is expressed as

$$\frac{m}{\tau}\frac{dr}{dt} = \frac{mv_\theta(r)^2}{r} - \frac{qV_{CPMA}}{r\ln\left(\frac{r_{2\_CPMA}}{r_{1\_CPMA}}\right)} , \tag{4}$$

and the trajectory equation is

$$\frac{dr}{dz} = \frac{dr}{dt}\left(\frac{dz}{dt}\right)^{-1} = \frac{c_r}{v_z} , \tag{5}$$

where τ is the relaxation time, m is the mass of the particle, t is time, V is the voltage difference between the two electrodes, and r_{1_CPMA} and r_{2_CPMA} are the radii of the inner and outer electrodes, respectively. c_r is the particle migration velocity, v_z is the axial flow distribution and v_θ is the velocity profile in the angular direction,

$$v_\theta = \omega_1 \frac{\hat{r}^2 - \hat{\omega}}{\hat{r}^2 - 1} r + \omega_1 r_{1\_CPMA}^2 \frac{\hat{\omega} - 1}{\hat{r}^2 - 1}\frac{1}{r} = \alpha r + \frac{\beta}{r} , \tag{6}$$

where $\hat{\omega} = \omega_2/\omega_1$ is the ratio of the rotational speed of the outer electrode to the inner electrode and ω_1 and ω_2 are the rotational speeds of the inner and outer electrodes, respectively. $\hat{r}$ is the ratio of the inner and outer radii.

Sipkens et al. (2019) presented methods to calculate the transfer function of the CPMA. They considered the Taylor series expansion about the center of the gap ($r_c=(r_{2\_\mathrm{CPMA}}+r_{1\_\mathrm{CPMA}})/2$) instead of the equilibrium radius to avoid problems with the scenario in which the equilibrium radius does not exist. This method is much simpler and more robust. In this case, the particle migration velocity in the radial direction is

$$c_r \approx C_3 + C_4(r - r_c) , \tag{7}$$

where

$$C_3 = \tau\left(\alpha^2 r_c + \frac{2\alpha\beta}{r_c} + \frac{\beta^2}{r_c^3} - \frac{C_0}{mr_c}\right) , \tag{8}$$

$$C_4 = \tau\left(\alpha^2 - \frac{2\alpha\beta}{r_c} - \frac{3\beta^2}{r_c^4} + \frac{C_0}{mr_c^2}\right) , \tag{9}$$

$$C_0 = \frac{qV_{CPMA}}{\ln(r_{2\_CPMA}/r_{1\_CPMA})} , \tag{10}$$

Assuming a plug flow, the transfer function would be

$$\Omega = \frac{r_b - r_a}{2\delta} , \tag{11}$$

where $\delta=(r_{2\_\mathrm{CPMA}}-r_{1\_\mathrm{CPMA}})/2$ is the half width of the gap between the two electrodes, and

$$r_a = \min\left\{r_{2\_CPMA}, max\left\{r_{1\_CPMA}, G_0\left(r_{1\_CPMA}\right)\right\}\right\}, \tag{12}$$

$$r_b = \min\left\{r_{2\_CPMA}, max\left\{r_{1\_CPMA}, G_0\left(r_{2\_CPMA}\right)\right\}\right\}, \tag{13}$$

$$G_0(r_L) = r_c + \left(r_L - r_c + \frac{C_3}{C_4}\right)\exp(-C_4 L\bar{v}) - \frac{C_3}{C_4}, \tag{14}$$

where $G_0(\mathrm{r})$ is the operator used to map the final radial position of the particle to its position at the inlet and $\bar{v}$ is the average flow velocity.

Reavell et al. (2011) calculated the resolution of the CPMA assuming that the gap between two electrodes is narrow enough that the variation of force in the gap can be ignored. The limiting mass can be calculated by

$$m_{n,min}^{n,max} - n \cdot m_1 = \pm\frac{Q_{CPMA}}{2\pi B_{n,min}^{n,max} L_{CPMA} r_c^2 \omega^2}, \tag{15}$$

where ω is the equivalent rotational speed calculated by $\omega = \alpha + \frac{\beta}{r_c^2}$, m_1 is the nominal mass that the CPMA can select, and $m_{n,min}^{n,max}$ and $B_{n,min}^{n,max}$ are the maximum and minimum mass and corresponding mobility of particles bearing number of elementary charges of n that the CPMA can select, respectively. Further details can be found in Reavell et al. (2011) and Sipkens et al. (2019).

AAC

The AAC classifies particles based on relaxation time, which is defined by

$$\tau = Bm = \frac{Cc(d_{ae})\rho_0 d_{ae}^2}{18\mu}, \tag{16}$$

where μ is the viscosity of air. $Cc(d_{ae})$ is the slip correction factor. ρ_0 is the standard density with a value of 1 g/cm^3 (Johnson et al. 2018). When the aerosol inlet flow rate equals the aerosol sampling outlet flow rate, it can be expressed as (Tavakoli and Olfert, 2013)

$$\Omega = \frac{1}{2\beta_{AAC}}\left[\left|\tilde{\tau} - (1 - \beta_{AAC})\right| + \left|\tilde{\tau} - (1 + \beta_{AAC})\right| - 2\left|\tilde{\tau} - 1\right|\right], \tag{17}$$

τ^* is the nominal relaxation time, which is classified by the AAC,

$$\tau^* = \frac{2Q_{sh}}{\pi\omega^2(r_{1\_AAC} + r_{\_2AAC})^2 L}, \tag{18}$$

where $\beta_{AAC} = \frac{Q_a}{Q_{sh}}$, $\tilde{\tau} = \frac{\tau}{\tau^*}$, r_{1_AAC} and r_{2_AAC} are the inner and outer radii of the AAC, respectively. The limiting τ that AAC can select are $(1 \pm \beta_{\mathrm{AAC}}) \cdot \tau^*$. The maximum and minimum values of d_{ae} can be derived and denote as $d_{\mathrm{ae,max}}$ and $d_{\mathrm{ae,min}}$, respectively.

2.2 Experimental setup

A schematic of the experimental setup is illustrated in Fig. 1. Soot particles were generated by a miniature inverted soot generator (Argonaut Scientific Ltd., Canada) with a propane flow of 74.8 SCPM and an air flow rate of 12 SLPM. Although this operation setting is not in the open-tip flame regime, the flame is open-tip consistent with Fig. 2d in Moallemi et al. (2019). Detailed aerosol generation methods can be found in Kazemimanesh et al. (2019b) and Moallemi et al. (2019). The polydispersed aerosols were dried to a relative humidity of <20% by a silica dryer and then passed through a soft X-ray neutralizer (Model 3088, TSI, Inc., USA). Five mobility diameters (80 nm, 100 nm, 150 nm, 200 nm and 250 nm) of soot particles were selected with the DMA (Model 3081, TSI Inc., USA, $Q_{sh}/Q_a = 10$). For the soot characterization, the monodisperse aerosol flow was switched between two parallel lines and fed into the CPMA (Cambustion Ltd., UK) and AAC (Cambustion, Ltd., UK, $Q_{sh}/Q_a = 10$); meanwhile, the condensation particle counter (CPC, Model 3756, TSI, Inc., USA, 0.3 $\text{L}\cdot\text{min}^{-1}$) was switched between the CPMA and AAC. The particle mass (m) and aerodynamic diameter (d_{ae}) were determined by the scanning mode of the CPMA and AAC, while the CPC recorded their corresponding number concentrations at each setpoint. For each d_m, the m and d_{ae} distributions were measured three times. Between measurements of each d_m, the CPC was used behind the DMA, and the number size distribution of the generated soot particles was measured by SMPS to ensure that the generated soot particles did not change during the whole experiment. The m and d_{ae} distributions were fitted to log-normal distributions; thus, the modes m and d_{ae} for the mobility-selected particles were determined. The equation of log-normal distribution used in this study is expressed as

$$N(d_p) = \frac{N_0}{\sqrt{2\pi}\ln\sigma}\exp\left(\frac{-(\ln(d_p)-\ln(\mu))^2}{2(\ln\sigma)^2}\right), \tag{19}$$

where σ is the geometric standard deviation and μ is the geometric mean.

The CPMA and AAC were calibrated with certified PSL spheres (Thermo, USA) with sizes of 70 nm, 150 nm and 303 nm before the measurement. The measured m and d_{ae} were compared to m_{PSL} and $d_{\text{ae, PSL}}$, which were calculated with the nominal diameter and density of PSL (1050 $\text{kg}\cdot\text{m}^{-3}$). The deviations between measured m and m_{PSL} or measured d_{ae} and $d_{\text{ae, PSL}}$ were 2.75% and 5.14%, respectively. To quantify the multiple charging effect of particles selected by the DMA-CPMA system, the soot particles were initially selected by the DMA-CPMA at different d_m and the corresponding m. Then, the d_{ae} distribution of mobility and mass selected particles was obtained by stepping the AAC rotation speed of the cylinder with simultaneous measurement of the particle concentration at the AAC outlet using a CPC (Fig. 1b).

3 Results and discussion

3.1 Transfer function of the tandem system

The DMA, PMA and AAC select particles based on the electrical diameter, mass and aerodynamic diameter, respectively. These properties can be connected as follows (Decarlo et al. 2004):

$$\frac{Cc(d_{ae})\rho_0 d_{ae}^2}{6} = \frac{Cc(d_m)\rho_{eff} d_m^2}{6} = m\frac{Cc(d_m)}{\pi d_m}, \tag{20}$$

The transfer function of the DMA-APM has been well documented and can be found in Kuwata (2015). The convolution of the transfer functions of the DMA-CPMA and DMA-AAC were calculated by the following equations.

$$\Phi_{\text{DMA-CPMA}} = \Omega_{CPMA}\Omega_{DMA}, \tag{21}$$

$$\Phi_{\text{DMA-AAC}} = \Omega_{DMA}\Omega_{AAC}, \tag{22}$$

where Φ and Ω are the transfer functions of each classification system expressed by subscripts. In the following discussion, we explain the transfer functions of the DMA-CPMA and DMA-AAC utilizing the literature data of soot particles (Pei et al., 2018). The d_m and m of the representative particles are 100 nm and

0.33 fg, respectively, and the corresponding d_{ae} is 68.3 nm according to Eq. (20). In the calculation, the following parameter set was employed: d_{m} = 80 nm, Q_{DMA} = 0.3 L min^{-1}, β_{DMA} = 0.1, m = 0.16 fg, Q_{CPMA}=0.3 L min^{-1}, R_{m} = 8, d_{ae} = 68.3 nm, Q_{AAC} = 0.3 L min^{-1}, β_{AAC} = 0.1. The transfer functions of DMA-CPMA and DMA-AAC were solved iteratively using logarithmically spaced d_{m}, m and d_{ae}, which included 600 points, respectively. The ranges of d_{m}, m and d_{ae} used in the calculations were from $<d_{\mathrm{m1,min}}$ to $>d_{\mathrm{m2,max}}$, from $<m_{\mathrm{1,min}}$ to $>m_{\mathrm{2,max}}$, from $<d_{\mathrm{ae,min}}$ to $>d_{\mathrm{ae,max}}$, respectively. The dimensions of the individual classifiers are summarized in Table 1.

DMA-CPMA

The DMA-CPMA transfer function is calculated in log(d_{m})-log(m) space, as shown in Fig. 2. In log(d_{m})-log(m) space, the mass–mobility relationship is

$$m = k_f (d_m/nm)^{D_{fm}} , \tag{23}$$

$$\log(m) = D_{\mathrm{fm}} \log(d_m/nm) + \log(k_f) , \tag{24}$$

In theory, D_{fm} equals 3 for spherical particles and smaller than 3 for aspherical particles. In the log(d_{m})-log(m) space, the relationship of m and d_{m} is linear, with the slope expressed as the mass–mobility exponent (D_{fm}) and the intercept representing the pre-exponential factor (k_f). Under this specific operation condition, no overlap was observed between the spherical particle population (black line) and the classification region for doubly charged particles, implying that only the singly charged particles were selected. For aspherical particles with $D_{\mathrm{fm}} < 3$, such as soot particles with aggregate structures, the particle population may overlap the doubly charged region when the slope (D_{fm}) is small enough; however, the combination of DMA and CPMA is generally used to avoid the multiple charge effect in soot studies. The reported D_{fm} values are typically in the range of 2.2–2.4 for fresh soot particles (Rissler et al., 2013) and diesel soot particles (Park et al., 2003). In the exemplary case (Pei et al., 2018), the derived D_{fm} of premixed flame-generated soot particles was 2.28, resulting in the particles population always going through the transfer area of doubly charged particles. This implies that the performance of the DMA-CPMA to eliminate multiply charged particles to a certain extent depends on the particle morphology.

The DMA-CPMA system can eliminate the multiply charged particles only if the D_{fm} of the particles is larger than the slope of a line connecting (d_{m}, m) = ($d_{\mathrm{m2,min}}$, $m_{\mathrm{2,max}}$)(d_{m1},m_{1}) (as PP$_0$ shown in Fig. 2). Since the CPMA is used downstream of the DMA, the value of the mass limit of particles with a certain mobility of B can be expressed as follows according to Eq. (15).

$$m_{n,min}^{n,max} = n \cdot m_1 \pm \frac{Q_{\mathrm{CPMA}}}{2\pi B L_{\mathrm{CPMA}} r_c^2 \omega^2} , \tag{25}$$

where $m_{n,min}^{n,max}$ is the maximum or minimum particle mass of particles with the mobility of B that would be selected by the CPMA. The subscript n is the charge quantity. Accordingly, the ideal condition to completely eliminate the multiply charged particles is

$$D_{fm} > PP_0 = \frac{\log(m_{2,max}/m_1)}{\log(d_{m2,min}/d_{m1})} = \frac{log\left(2+\frac{1}{R_m(1+\beta_{DMA})}\right)}{log\left(\frac{2}{(1+\beta_{DMA})}\frac{Cc(d_{m2,min})}{Cc(d_{m1})}\right)} \tag{26}$$

The ability of the DMA-CPMA to eliminate multiply charged particles depends on the selected d_m, m and resolutions of both the DMA and CPMA. Eq. (26) gives instructions in actual operation to eliminate multiply charged particles. When selecting particles of certain d_m and m, by decreasing Q_CPMA, or increasing ω and β_DMA, i.e., by increasing the resolution of the measurement, the potential of multiply charged particles is reduced. Thus, the key to evaluating whether there is a multiple charging effect lies in the particle morphology (D_fm) and the slope of PP_0 derived from the actual condition. Compared with the DMA-CPMA, the selection of the DMA-APM is more susceptible to multiple charging effect. According to the theoretical calculation described in Kuwata (2015), the slope of PP_0 of 3.55 was derived when the DMA-APM selects the same example soot particles from Pei et al. (2018) (d_m of 100 nm and m of 0.33 fg) with a D_fm of 2.28, indicating that the DMA-APM is more subject to the multiple charging effect.

In addition to the instrument setup, the particle morphology is also crucial for the DMA-CPMA. Here, we simulate the critical slope of PP_0 when selecting different d_m and m under the common selecting conditions ($\beta_\mathrm{DMA} = 0.1$, Q_CPMA=0.3 L min^{-1}, $R_\mathrm{m} = 8$), which is represented as contour lines in Fig. 3 (A black and white version is shown as Fig. S4) . Under these selection conditions, the DMA-CPMA can select monodispersed particles when the D_fm of the particles is larger than the critical slope of PP_0. When selecting small aspherical particles or particles with extremely low density, the slope of PP_0 is relatively higher, and the DMA-CPMA classification is sensitive to multiple charging effect. As shown in Fig. 3, d_m, m and the corresponding D_fm were taken from the literature (Park et al., 2003; Rissler et al., 2013; Tavakoli et al., 2014; Ait Ali Yahia et al., 2017; Dastanpour et al., 2017; Forestieri et al., 2018; Pei et al., 2018; Kazemimanesh et al., 2019a). Generally, for soot particles with D_fm of 2.2-2.4, the multiple charging effect can be avoided for the DMA-CPMA when selecting soot particles with mobility diameters larger than 200 nm, while it fails to eliminate multiply charged particles when selecting small soot particles. These potential uncertainties are discussed in detail with flame-generated soot particles in Sect. 3.2.

DMA-AAC

The advantage of the AAC versus the CPMA is that there is no need for a neutralizer to charge aerosol particles. Measuring solely with an AAC will avoid multiple charging. However, AAC cannot constrain the properties of aspherical particles as monodisperse as DMA or CPMA classification (Kazemimanesh et al., 2022). Multiple charging becomes a problem when the tandem measurement is made with a DMA or PMA. The transfer function of the DMA-AAC selecting the same representative particles was calculated and is shown in log(d_ae)-log(d_m) (Fig. 4a). Moreover, according to Eq. 20 and Eq. 23, aspherical particles can be expressed as follows:

$$logd_{ae} = \frac{1}{2}\left(D_{fm} - 1\right)logd_m + \frac{1}{2}\log\left(\frac{6}{\pi}\frac{Cc(d_m)k_f}{Cc(d_{ae})\rho_0}\cdot 10^{9D_{fm}-18}\right), \qquad (27)$$

which indicates that the relationship between d_ae and d_m is nonlinear since $Cc(d_\mathrm{m})$ and $Cc(d_\mathrm{ae})$ vary with d_m and d_ae, respectively. Particle morphology can be derived from the relationship between d_m and d_ae measured by a DMA and AAC, respectively. To simulate the transfer function of the DMA-AAC, the same particles as those used in the calculations of the DMA-CPMA were selected. The corresponding d_ae was numerically solved using the known mass–mobility relationship. Unlike the DMA-CPMA system, the transfer functions of singly charged and doubly charged particles are in parallel for the DMA-AAC, suggesting that the particles population is less likely to overlap with the region of multiply charged particles. Using the example setups of the DMA-AAC, truly monodispersed particles are selected for spherical particles and typical soot particles. Similar to the DMA-CPMA system, eliminating multiply charged particles requires that the $d_{\mathrm{ae,max}}$ of the AAC at $d_{\mathrm{m2,min}}$ must be smaller than the d_{ae} of particles of interest, which can be derived from $d_{\mathrm{m2,min}}$ and D_{fm} (Eq. 27),

$$d_{ae}\left(d_{m2,min}, D_{fm}\right) > d_{ae,max}\left(d_{m2,min}\right) ,$$

$$\Rightarrow D_{fm} > \frac{\log(2\cdot\frac{1+\beta_{AAC}}{1+\beta_{DMA}})}{\log[\frac{2}{1+\beta_{DMA}}\cdot\frac{Cc\left(d_{m2,min}\right)}{Cc(d_{m1})}]} , \tag{28}$$

This equation describes the minimum value of D_{fm} to eliminate the multiple charging effect. It is clearly shown that the mobility resolution of the DMA and the relaxation time resolution of the AAC determine the limiting condition, and the resolution of the AAC is more important compared with the resolution of the DMA. The limiting condition is also related to the selected d_{m} of the DMA but independent of the selected d_{ae} of the AAC (Fig. S1). Setting the same resolutions for the DMA and AAC, particle selection is more susceptible to multiple charging effects when selecting small sizes. In Fig. 4a, the values of β_{DMA} and β_{AAC} are 0.1, resulting in a minimum D_{fm} of 1.41, which is the case for most atmospheric aerosol particles. Hence, the selected particles of the DMA-AAC are truly monodisperse regardless of the particle morphology. However, in actual operations, a larger sample flow rate is required to satisfy the apparatus downstream, while the maximum sheath flow rate of the classifier is restricted by the instrument design (e.g., 30 L min^{-1} for the DMA and 15 L min^{-1} for the AAC). In addition, the maximum size ranges are also restricted by the sheath flow, so in some cases, a lower sheath flow rate is required to select larger particles. When increasing β_{AAC} to 0.3 and leaving β_{DMA} unchanged, the transfer function becomes broader (Fig. 4b). The minimum D_{fm} is 2.44, which indicates that the multiple charging effect exists for typical soot particles with D_{fm} of 2.2-2.4. The line representing soot particles overlaps with the region of doubly charged particles. Thus, reducing the resolutions of the DMA or AAC is not suggested in actual operations.

3.2 Evaluation of the multiple charging effect

To quantify the possible biases of the multiple charging effect in the DMA-CPMA system, we conducted a soot experiment, as demonstrated in Fig. 1. For each mobility-selected particles, the corresponding d_{ae} and m were determined using the AAC and CPMA scan modes, from which the effective densities were derived. Representative plots for the measured spectral density of mass and aerodynamic diameter of particles with d_{m} of 150 nm and 250 nm are shown in Fig. S2. The results are summarized in Table 2. The fitted values of D_{fm} and k_f were 2.28 and 7.49×10^{-6}, respectively, indicating a fractal structure, which is the same as in previous studies (Pei et al., 2018). The effective densities of generated soot particles vary from >500 kg m^{-3} at d_{m} = 80 nm to <300 kg m^{-3} at d_{m} of 250 nm for the two methods. In general, the deviation monotonically decreases with increasing particle size. The deviation is 7.65% for particles of 80 nm, whereas it decreased to <1% for particles larger than 200 nm. The results reveal a strict agreement between the two methods for retrieving the particle effective density.

According to Fig. 3, the critical slopes of PP_0 for soot particles with d_m of 80 nm, 100 nm, 150 nm, 200 nm and 250 nm are 2.46, 2.41, 2.29, 2.17 and 2.08, respectively. The measured D_{fm} of 2.28 is smaller than the calculated PP_0 for particles with d_m smaller than 200 nm, which suggests that the contributions from the multiply charged particles cannot be eliminated.

When selecting particles with d_m of 80 nm and m of 0.16 fg, the corresponding transfer function is shown in Fig. 5a. The particle population overlaps the transfer function region of doubly charged particles, suggesting the potential interferences of doubly charged particles in DMA-CPMA selection. Since the classification of the AAC is different from the DMA and CPMA, the aerodynamic size distributions of mobility and mass selected particles were characterized. Fig. 5b shows the particles number aerodynamic size distribution ($PNSD_{ae}$) scanned by the AAC. $PNSD_{ae}$ was fitted using log-normal distributions, and three peaks corresponding to singly, doubly and triply charged particles were identified. Some small particles remaining in the AAC induced the peak at d_{ae} <40 nm. These residual particles were measured even if the sample flow was filtered. The mean d_{ae} values were 53.9 nm, 60.6 nm and 70.9 nm, and the corresponding d_{ae} values were calculated as 51.5 nm, 62.0 nm and 70.7 nm using Eq. (1) and Eq. (16). The experimental results are consistent with the theoretical results with deviations within 5.3%.

In contrast, when selecting particles with d_m of 200 nm and m of 1.28 fg, the transfer function is shown in Fig. 6a. The PP_0 slope of 2.17 is smaller than that D_{fm} of 2.28, and the generated particles population does not overlap with the block of doubly charged particles; thus, the DMA-CPMA classified particles were truly monodispersed. $PNSD_{ae}$ measured by the AAC is unimodal, implying that the classified particles were singly charged (Fig. 6b).

The results of other experiments are shown in Fig. S3. Although the critical slope of PP0 when selecting 150 nm particles is close to D_{fm} and the transfer function of DMA-CPMA also showed that negligible multiply charged particles would be selected (Fig. S3d), doubly charged particles were measured in $PNSD_{ae}$ (Fig. S3e). These doubly charged particles were selected, probably owing to particle diffusion. The nondiffusion models were used to calculate the transfer function, but the transfer function can be broader because of diffusion. In summary, for a type of particle with the same mass–mobility relationship, the possibility of multiple charging increases for small particles when selected by the DMA-CPMA system, which is consistent with the theoretical calculation in Sect. 3.1.

3.3 Atmospheric implication

The DMA-APM and DMA-CPMA systems are usually adopted to eliminate multiply charged particles in soot aerosol studies. Although they might fail to select monodispersed particles, downstream measurements by instruments such as a single-particle soot photometer (SP2) will not be interfered with, which characterizes the distinct information of a single particle. Nevertheless, for techniques measuring the properties of an entire aerosol population, e.g., scattering coefficient by a nephelometer or absorption coefficient by a photoacoustic spectrometer, multiply charged particles can induce significant bias. A previous study (Radney and Zangmeister, 2016) noted that the DMA-APM failed to resolve multiply charged particles for soot particles when selecting 150 nm flame-generated particles, which caused a 110% error in extinction measurement. To investigate the multiple charging effect for DMA-CPMA classification, the optical absorption coefficient of particles with different charging states after DMA-CPMA classification was calculated from $\mathrm{PNSD_{ae}}$. Mie theory was used to calculate the theoretical absorption coefficient at a wavelength of 550 nm. Mie theory is probably not the "best" method to use here since soot particles are aspherical agglomerates. Realistically, however, the Mie comparison is only being used to prove a point about the impact of multiple charging. Therefore, in this instance, any errors in the calculated optical properties are somewhat inconsequential. The refractive index used in the Mie code was 1.95+0.79i (Bond and Bergstrom, 2006). The $\mathrm{PNSD_{ae}}$ for different charging state particles was converted to volume-equivalent diameter size distributions ($\mathrm{PNSD_{ve}}$), which was used in Mie theory to determine the absorption coefficient. The method to calculate $\mathrm{PNSD_{ve}}$ is described in Sect. S1. Subsequently, the absorption coefficient, α_{abs}, was derived using Mie theory and the $\mathrm{PNSD_{ve}}$ of particles with different charging states. For soot particles with diameters <200 nm, the optical absorption contributions of particles with different charging states and the mass absorption cross-section (MAC) overestimation are summarized in Table 3. For soot particles with a diameter of 80 nm, the contributions of particles with different charging states are shown in Fig. 5c. Doubly charged particles only account for 26.7±3.0% of the total number concentration but provide a large fractional contribution to the total absorption (45.7±4.2%). Additionally, a small fraction (1.1±0.4%) of triply charged particles accounted for 3.7±1.5% of the absorption. As a result, the MAC was overestimated by 43.0±2.7%, and the directive radiative force (DRF) was overestimated by 43.0±2.7%. The DRF was calculated using previous global climate models (Bond et al., 2016). For particles selected by the DMA-CPMA at a d_{m} of 200 nm and an m of 1.28 fg, the selected particles were truly dispersed, and the measured optical properties were valid (Fig. 6c).

A large amount of 70 nm -90 nm soot particles was emitted from diesel engine (Wierzbicka et al., 2014), and neglecting the multiple charging effect in the measurement of mass-specific MAC on this size range will result in significant bias in the estimation of radiative forcing of automobile-emitted soot particles, which may lead to large errors in climate model.

According to Table 3, the number fraction of doubly charged particles declines with the size of the nominated particles, i.e., 26.7±3.0% and 17.6±0.5% for 80 and 100 nm particles, respectively, but only 4.2±1.1% for 150 nm particles. Accordingly, the MAC was largely overestimated for 80 and 100 nm particles (43.0±2.7% and 27.9±0.8%, respectively) but moderately overestimated for 150 nm particles (9.3±2.6%). To summarize, our results indicated that the combination of tandem classifiers is not sufficient to completely eliminate multiply charged particles when selecting small flame-generated soot particles, which introduced noticeable bias for absorption measurements and led to overestimation of the MAC. As a result, the DRF of soot particles was also overestimated.

4 Conclusion

In this study, we demonstrate the transfer functions of DMA-CPMA and DMA-AAC and discuss their limitations to eliminate multiply charged particles. For aspherical particles, there is no guarantee that the multiple charging effect can be avoided in DMA-CPMA or DMA-AAC systems. Usually, a DMA-AAC can select truly monodisperse particles, but the method can suffer from multiple charging when decreasing the resolutions of the DMA and AAC. The ability of the DMA-CPMA to eliminate multiple charging effect mainly depends on the particle morphology and the instrument resolutions. Under the same setups of DMA-CPMA, this tandem system is more sensitive to multiple charging effect with decreasing D_{fm} and decreasing nominal size of particles. The DMA-CPMA failed to eliminate multiply charged particles when selecting soot particles with diameters < 150 nm. Although doubly charged particles accounted for a small fraction of the number concentration, they contributed most significantly to light absorption, which indicated that multiply charged particles can induce an obvious contribution to light absorption and lead to an overestimation of DRF for flame-generated soot particles.

Code/Data availability. Code/Data are available upon request.

Author contributions. ZW determined the main goal of this study. YS and XP designed the methods. YS carried them out and prepared the paper with contributions from all coauthors. YS, HL and JZ analyzed the optical data.

Competing interests. The authors declare that they have no conflicts of interest.

Acknowledgments. The study was supported by the National Natural Science Foundation of China (91844301 and 41805100).We especially acknowledge useful comments and suggestions on the MATLAB script of the CPMA transfer function from Timothy A. Sipkens.

Appendix A

Table A1. Symbols used in this study

μ	Air viscosity
β	The ratio of flow rates of aerosol flow and sheath flow, $Q_{\mathrm{a}}/Q_{\mathrm{sh}}$
τ	Relaxation time
ω_1	Rotational speed of the inner electrode
ω_2	Rotational speed of the outer electrode
$\widehat{\omega}$	$\omega_1/\ \omega_2$
δ	Half width of the gap between the two electrodes
Ω	Transfer function
ρ_0	Standard density, which equals 1 kg/m^3
τ	Relaxation time

τ^*	τ at the maximum of the transfer function
$\tilde{\tau}$	Dimensionless particle relaxation time, $\tilde{\tau} = \tau/\tau^*$
ρ_{eff}	Effective density
k_{f}	Mass-mobility pre-exponential factor
α_{abs}	Absorption coefficient
B	Mechanical mobility
$C_{\mathrm{c}}(d_{\mathrm{p}})$	Cunningham slip correction factor
c_{r}	Particle migration velocity
D_{fm}	Mass-mobility exponent
d_{ae}	Aerodynamic equivalent diameter
d_m	Mobility equivalent diameter
d_{ve}	Volume-equivalence size
e	Elementary charge
L	Length of DMA, CPMA or AAC
m	Particle mass
n	Number of elementary charges on the particle
PNSD	Particle number size distribution
$\mathrm{PNSD}_{\mathrm{ae}}$	Particle number aerodynamic size distribution
$\mathrm{PNSD}_{\mathrm{ve}}$	Particle number volume-equivalent size distribution
Q_{a}	Sample flow rate
Q_{sh}	Sheath flow rate
q	Electrical charge on the particle
R_{m}	Mass resolution of CPMA
r_{a}	Lower initial radial position that passes through the classifier
r_{b}	Upper initial radial position that passes through the classifier
r_1	Inner radium
r_2	Outer radium
$\hat{r}$	r_1/r_2
t	Time
V	Voltage between the two electrodes of DMA or CPMA
$\bar{v}$	Average flow velocity
v_{z}	Axial flow distribution
v_{θ}	Velocity profile in the angular direction
Z_{p}*	Z_{p} at the maximum transfer function of DMA
Z_{p}	Electrical mobility
$\tilde{Z}_p$	$Z_p/Z_p{}^*$

References

Ait Ali Yahia, L., Gehin, E., and Sagot, B.: Application of the The Rmophoretic Annular Precipitator (TRAP) for the study of soot aggregates morphological influence on their thermophoretic behaviour, J. Aerosol Sci., 113, 40-51, https://doi.org/10.1016/j.jaerosci.2017.07.018, 2017.

Biskos, G., Malinowski, A., Russell, L. M., Buseck, P. R., and Martin, S. T.: Nanosize Effect on the Deliquescence and the Efflorescence of Sodium Chloride Particles, Aerosol Sci. Technol., 40, 97-106, https://doi.org/10.1080/02786820500484396, 2006.

Bond, T. C., and Bergstrom, R. W.: Light Absorption by Carbonaceous Particles: An Investigative Review, Aerosol Sci. Technol, 40, 27-67, https://doi.org/10.1080/02786820500421521, 2006.

Bond, T. C., Doherty, S. J., Fahey, D. W., Forster, P. M., Berntsen, T., DeAngelo, B. J., Flanner, M. G., Ghan, S., Kärcher, B., Koch, D., Kinne, S., Kondo, Y., Quinn, P. K., Sarofim, M. C., Schultz, M. G., Schulz, M., Venkataraman, C., Zhang, H., Zhang, S., Bellouin, N., Guttikunda, S. K., Hopke, P. K., Jacobson, M. Z., Kaiser, J. W., Klimont, Z., Lohmann, U., Schwarz, J. P., Shindell, D., Storelvmo, T., Warren, S. G., and Zender, C. S.: Bounding the role of black carbon in the climate system: A scientific assessment, J. Geophys. Res.: Atmos.: Atmospheres, 118, 5380-5552, https://doi.org/10.1002/jgrd.50171, 2013.

Cheng, Y., Su, H., Koop, T., Mikhailov, E., and Pöschl, U.: Size dependence of phase transitions in aerosol nanoparticles, Nat. Commun., 6, https://doi.org/10.1038/ncomms6923, 2015.

Dastanpour, R., Momenimovahed, A., Thomson, K., Olfert, J., and Rogak, S.: Variation of the optical properties of soot as a function of particle mass, Carbon, 124, 201-211, https://doi.org/10.1016/j.carbon.2017.07.005, 2017.

Dusek, U., Frank, G. P., Hildebrandt, L., Curtius, J., Schneider, J., Walter, S., Chand, D., Drewnick, F., Hings, S., Jung, D., Borrmann, S., and Andreae, M. O.: Size Matters More Than Chemistry for Cloud-Nucleating Ability of Aerosol Particles, Science, 312, 1375-1378, https://doi.org/10.1126/science.1125261, 2006.

Ehara, K., Hagwood, C., and Coakley, K. J.: Novel method to classify aerosol particles according to their mass-to-charge ratio—Aerosol particle mass analyser, J. Aerosol Sci, 27, 217-234, https://doi.org/10.1016/0021-8502(95)00562-5, 1996.

Johnson, T. J., Nishida, R., Irwin, M., Symonds, J. P.R., Olfert, J. S., Boies, A.: Agreement Between Different Aerosol Classifiers Using Spherical Particles, https://doi.org/10.13140/RG.2.2.30999.27043, 2018.

Johnson, T. J.; Nishida, R. T.; Zhang, X.; Symonds, J. P. R.; Olfert, J. S.; Boies, A. M., Generating an aerosol of homogeneous, non-spherical particles and measuring their bipolar charge distribution. J. Aerosol Sci, 153. https://doi.org/10.1016/j.jaerosci.2020.105705, 2021.

Johnson, T. J.; Olfert, J. S.; Cabot, R.; Treacy, C.; Yurteri, C. U.; Dickens, C.; McAughey, J.; Symonds, J. P. R., Steady-state measurement of the effective particle density of cigarette smoke. J. Aerosol Sci, 75, 9-16, https://doi.org/10.1016/j.jaerosci.2014.04.006, 2014.

Kazemimanesh, M., Dastanpour, R., Baldelli, A., Moallemi, A., Thomson, K. A., Jefferson, M. A., Johnson, M. R., Rogak, S. N., and Olfert, J. S.: Size, effective density, morphology, and nano-structure of soot particles generated from buoyant turbulent diffusion flames, J. Aerosol Sci., 132, 22-31, https://doi.org/10.1016/j.jaerosci.2019.03.005, 2019a.

Kazemimanesh, M., Moallemi, A., Thomson, K., Smallwood, G., Lobo, P. and Olfert, J.S.: A novel miniature inverted-flame burner for the generation of soot nanoparticles. Aerosol Sci. and Technol., 53(2), 184-195, https://doi.org/10.1080/02786826.2018.1556774, 2019b.

Kazemimanesh, M., Rahman, M.M., Duca, D., Johnson, T.J., Addad, A., Giannopoulos, G., Focsa, C. and Boies, A.M.: A comparative study on effective density, shape factor, and volatile mixing of non-spherical particles using tandem aerodynamic diameter, mobility diameter, and mass measurements. J. Aerosol Sci., 161, 105930, https://doi.org/10.1016/j.jaerosci.2021.105930, 2022.

Knutson, E. O., and Whitby, K. T.: Aerosol classification by electric mobility: apparatus, theory, and applications, J. Aerosol Sci., 6, 443-451, https://doi.org/10.1016/0021-8502(75)90060-9, 1975.

Kuwata, M.: Particle Classification by the Tandem Differential Mobility Analyzer–Particle Mass Analyzer System, Aerosol Sci. Technol., 49, 508-520, https://doi.org/10.1080/02786826.2015.1045058, 2015.

Moallemi, A.; Kazemimanesh, M.; Corbin, J. C.; Thomson, K.; Smallwood, G.; Olfert, J. S.; Lobo, P., Characterization of black carbon particles generated by a propane-fueled miniature inverted soot generator. J. Aerosol Sci., 135, 46-57, https://doi.org/10.1016/j.jaerosci.2019.05.004, 2019.

Olfert, J. S., and Collings, N.: New method for particle mass classification—the Couette centrifugal particle mass analyzer, J. Aerosol Sci., 36, 1338-1352, https://doi.org/10.1016/j.jaerosci.2005.03.006, 2005.

Park, K., Cao, F., Kittelson, D. B, and Mcmurry, P. H.: Relationship between Particle Mass and Mobility for Diesel Exhaust Particles, Environ. Sci. & Technol., 37, 577-583, https://doi.org/10.1021/es025960v, 2003.

Park, K., Dutcher, D., Emery, M., Pagels, J., Sakurai, H., Scheckman, J., Qian, S., Stolzenburg, M. R., Wang, X., Yang J., and McMurry P. H.: Tandem Measurements of Aerosol Properties—A Review of Mobility Techniques with Extensions. Aerosol Sci. and Techno., 42, 801-816, https://doi.org/10.1080/02786820802339561, 2008.

Pei, X., Hallquist, M., Eriksson, A. C., Pagels, J., Donahue, N. M., Mentel, T., Svenningsson, B., Brune, W., and Pathak, R. K.: Morphological transformation of soot: investigation of microphysical processes during the condensation of sulfuric acid and limonene ozonolysis product vapors, Atmos. Chem. Phys., 18, 9845-9860, https://doi.org/10.5194/acp-18-9845-2018, 2018.

Radney, J. G., Ma, X., Gillis, K. A., Zachariah, M. R., Hodges, J. T., and Zangmeister, C. D.: Direct Measurements of Mass-Specific Optical Cross Sections of Single-Component Aerosol Mixtures, Anal. Chem., 85, 8319-8325, https://doi.org/10.1021/ac401645y, 2013.

Radney, J. G., and Zangmeister, C. D.: Practical limitations of aerosol separation by a tandem differential mobility analyzer–aerosol particle mass analyzer, Aerosol Sci. Technol., 50, 160-172, https://doi.org/10.1080/02786826.2015.1136733, 2016.

Rissler, J., Messing, M. E., Malik, A. I., Nilsson, P. T., Nordin, E. Z., Bohgard, M., Sanati, M., and Pagels, J. H.: Effective Density Characterization of Soot Agglomerates from Various Sources and Comparison to Aggregation Theory, Aerosol Sci. Technol., 47, 792-805, 10.1080/02786826.2013.791381, 2013.

Shiraiwa, M., Kondo, Y., Iwamoto, T., and Kita, K.: Amplification of Light Absorption of Black Carbon by Organic Coating, Aerosol Sci. & Technol., 44, 46-54, https://doi.org/10.1080/02786820903357686, 2010.

Sipkens, T. A., Olfert, J. S., and Rogak, S. N.: New approaches to calculate the transfer function of particle mass analyzers, Aerosol Sci. Technol., 54, 111-127, https://doi.org/10.1080/02786826.2019.1680794, 2019.

Stolzenburg, M. R., and McMurry, P. H.: Equations Governing Single and Tandem DMA Configurations and a New Lognormal Approximation to the Transfer Function, Aerosol Sci. Technol., 42, 421-432, https://doi.org/10.1080/02786820802157823, 2008.

Swietlicki, E., Hansson, H. C., Hämeri, K., Svenningsson, B., Massling, A., McFiggans, G., McMurry, P. H., Petäjä, T., Tunved, P., Gysel, M., Topping, D., Weingartner, E., Baltensperger, U., Rissler, J., Wiedensohler, A., and Kulmala, M.: Hygroscopic properties of submicrometer atmospheric aerosol particles measured with H-TDMA instruments in various environments – a review, Tellus B, 60, 432–469, https://doi.org/10.1111/j.1600-0889.2008.00350.x, 2008.

Tavakoli, F., and Olfert, J. S.: An Instrument for the Classification of Aerosols by Particle Relaxation Time: Theoretical Models of the Aerodynamic Aerosol Classifier, Aerosol Sci. Technol., 47, 916-926, https://doi.org/10.1080/02786826.2013.802761, 2013.

Tavakoli, F., and Olfert, J. S.: Determination of particle mass, effective density, mass–mobility exponent, and dynamic shape factor using an aerodynamic aerosol classifier and a differential mobility analyzer in tandem, J. Aerosol Sci., 75, 35-42, https://doi.org/10.1016/j.jaerosci.2014.04.010, 2014.

Wiedensohler, A., Birmili, W., Nowak, A., Sonntag, A., Weinhold, K., Merkel, M., Wehner, B., Tuch, T., Pfeifer, S., Fiebig, M., Fjäraa, A. M., Asmi, E., Sellegri, K., Depuy, R., Venzac, H., Villani, P., Laj, P., Aalto, P., Ogren, J. A., Swietlicki, E., Williams, P., Roldin, P., Quincey, P., Hüglin, C., Fierz-Schmidhauser, R., Gysel, M., Weingartner, E., Riccobono, F., Santos, S., Grüning, C., Faloon, K., Beddows, D., Harrison, R., Monahan, C., Jennings, S. G., O'Dowd, C. D., Marinoni, A., Horn, H.-G., Keck, L., Jiang, J., Scheckman, J., McMurry, P. H., Deng, Z., Zhao, C. S., Moerman, M., Henzing, B., de Leeuw, G., Löschau, G., and Bastian, S.: Mobility particle size spectrometers: harmonization of technical standards and data structure to facilitate high quality long-term observations of atmospheric particle number size distributions, Atmos. Meas. Tech., 5, 657–685, https://doi.org/10.5194/amt-5-657-2012, 2012.

Yao, Q., Asa-Awuku, A., Zangmeister, C. D., and Radney, J. G.: Comparison of three essential sub-micrometer aerosol measurements: Mass, size and shape, Aerosol Sci. Technol., 1-18, https://doi.org/10.1080/02786826.2020.1763248, 2020.

Zangmeister, C. D., You, R., Lunny, E. M., Jacobson, A. E., Okumura, M., Zachariah, M. R., and Radney, J. G.: Measured in-situ mass absorption spectra for nine forms of highly-absorbing carbonaceous aerosol, Carbon, 136, 85-93, https://doi.org/10.1016/j.carbon.2018.04.057, 2018.

Zhang, R., Khalizov, A. F., Pagels, J., Zhang, D., Xue, H., and McMurry, P. H.: Variability in morphology, hygroscopicity, and optical properties of soot aerosols during atmospheric processing, Proc. Natl. Acad. Sci., 105, 10291, https://doi.org/10.1073/pnas.0804860105, 2008.

Table 1 Dimensions of the three classifiers used for transfer function calculation

Parameter	DMA	CPMA	AAC
r_1 (mm)	9.37	100	43
r_2 (mm)	19.61	103	45
L (mm)	44.369	200	210
ω_2/ω_1	—	0.945	—

Table 2. Mobility diameter, mass, aerodynamic diameter, effective densities calculated by DMA-AAC and DMA-CPMA, and the deviation between them for fresh soot particles in the size range of 80–250 nm.

d_m (nm)	M (fg)	d_{ae} (nm)	$\rho_{DMA\text{-}AAC}$ (kg m^{-3})	$\rho_{DMA\text{-}CPMA}$ (kg m^{-3})	Deviation
80	0.16±0.01	48.2±0.3	551.2±6.9	596.8±37.30	7.65%
100	0.27±0.01	54.8±0.3	488.0±5.32	515.7±19.10	5.38%
150	0.66±0.07	67.8±0.3	359. 1±3.22	373.5±39.61	3.86%
200	1.28±0.10	82.1±0.6	303.2±4.44	305.6±23.87	0.77%
250	2.17±0.16	95.9±0.9	262.8±4.92	265.2±19.56	0.90%

Table 3. Number concentration fractions and absorption contributions for different size fresh soot particles with single, double or triple charges and the overestimation of MAC accordingly.

d_m (nm)	singly charged particles		doubly charged particles		triply charged particles		MAC overestimation
	f_N(%)	f_{abs}(%)	f_N(%)	f_{abs}(%)	f_N(%)	f_{abs}(%)	
80	72.2±2.5	50.6±2.7	26.7±3.0	45.7±4.2	1.1±0.4	3.7±1.5	43.0±2.7
100	82.4±0.5	64.4±0.8	17.6±0.5	35.6±0.8	-	-	27.9±0.8
150	95.8±1.2	87.7±3.1	4.2±1.1	12.3±3.1	-	-	9.3±2.6

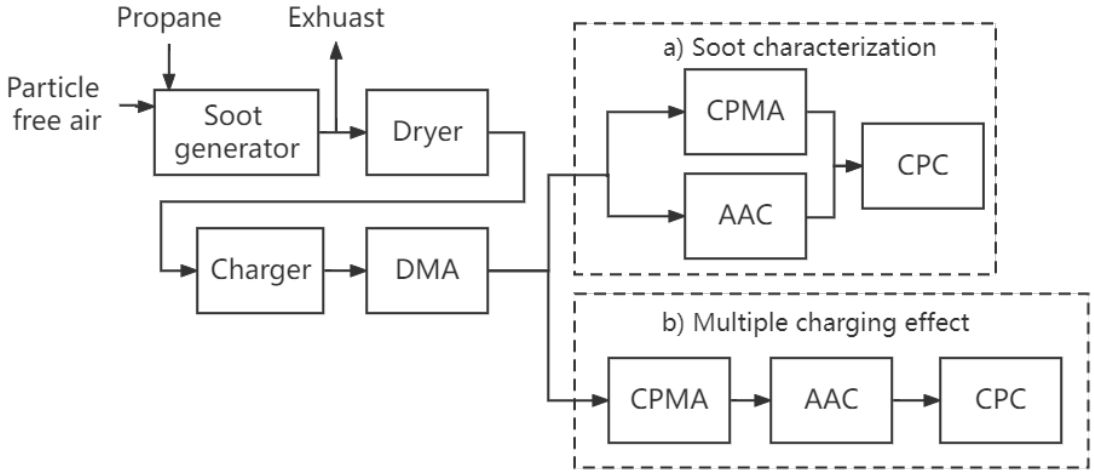

Figure 1: Schematic of the experimental setup: (a) soot characterization and (b) evaluation of multiple charging effects.

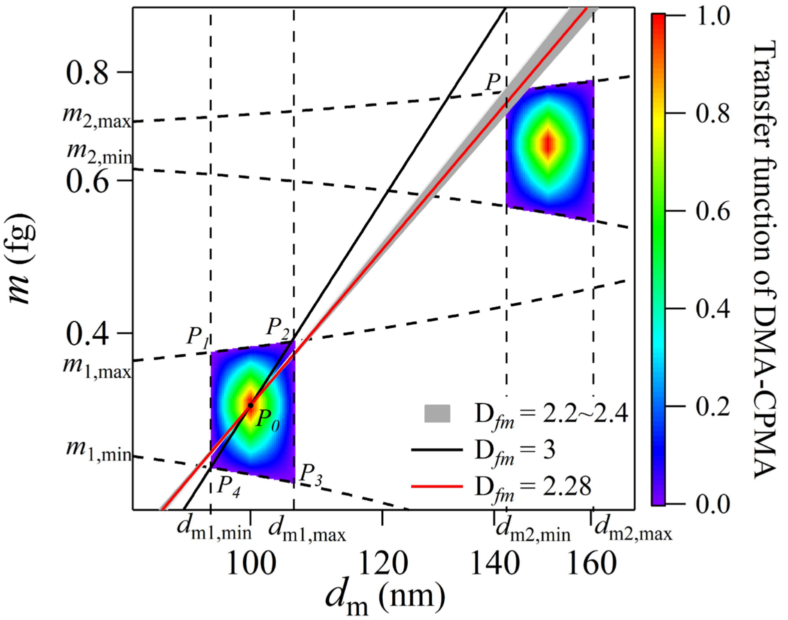

Figure 2: Example of the DMA-CPMA transfer function of flame-generated soot particles (Pei et al., 2018). The following parameter set was employed for the calculations: d_m = 100 nm, β_{DMA} = 0.1, m = 0.33 fg, Q_{CPMA}=0.3 L min^{-1}, R_m = 8. The color blocks are the transfer function of DMA-CPMA, with the rainbow color representing the transfer function for singly charged (lower left block) and doubly charged (upper right block) particles. The black and red solid lines are particles populations with D_{fm} values of 3 and 2.28, respectively. The gray region is the particle population with D_{fm} of 2.2-2.4, which is typical for soot aerosols. The dashed lines are the limits of d_m and m of DMA and CPMA. The DMA–CPMA transfer function for +2 particles does not overlap with the line for spherical particles with a single charge (D_{fm}=3).

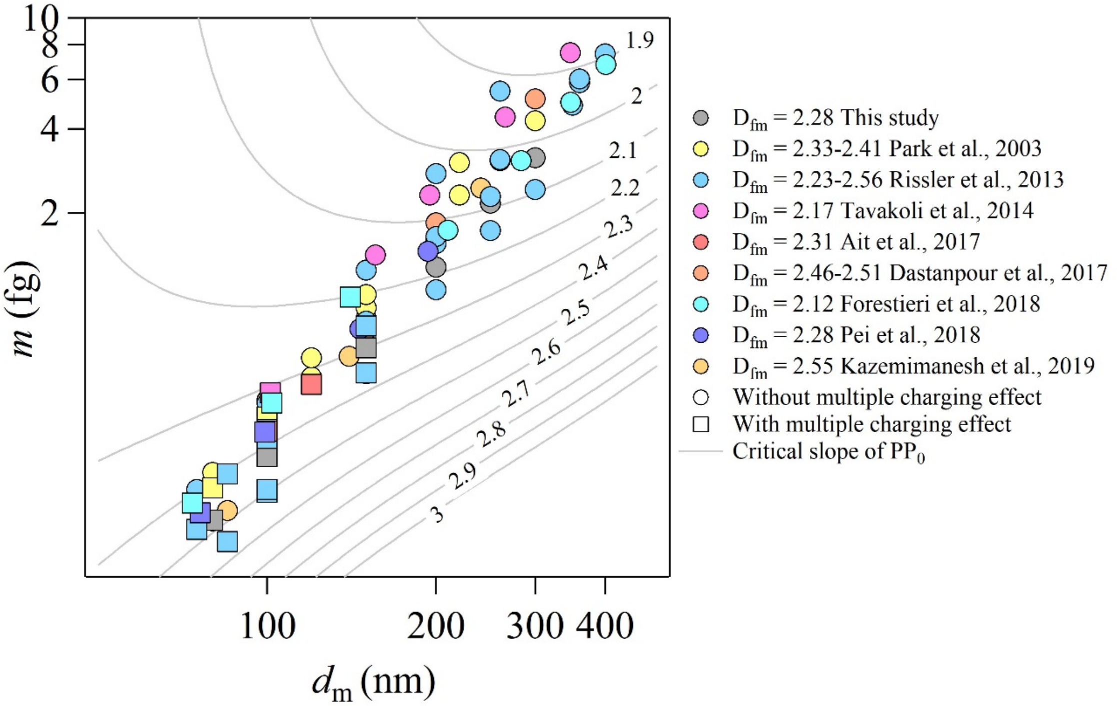

Figure 3: Variations of the slope of PP_0 as a function of classified d_m and m. The following parameter set was employed for the calculations: β_{DMA} = 0.1, Q_{CPMA}=0.3 L min^{-1}, R_m = 8. The contour lines denote the slope of PP_0, with values labeled on them. The data points are soot particles measured in the literature (Park et al., 2003; Rissler et al., 2013; Tavakoli et al., 2014; Ait Ali Yahia et al., 2017; Dastanpour et al., 2017; Forestieri et al., 2018; Pei et al., 2018; Kazemimanesh et al., 2019) and generated in this study (see details in Sect 3.2). The D_{fm} values of these data points are listed in the legend. The data points become square when D_{fm} is smaller than the critical slope of PP0 in the background, i.e., the potential multiple charging effect may exist.

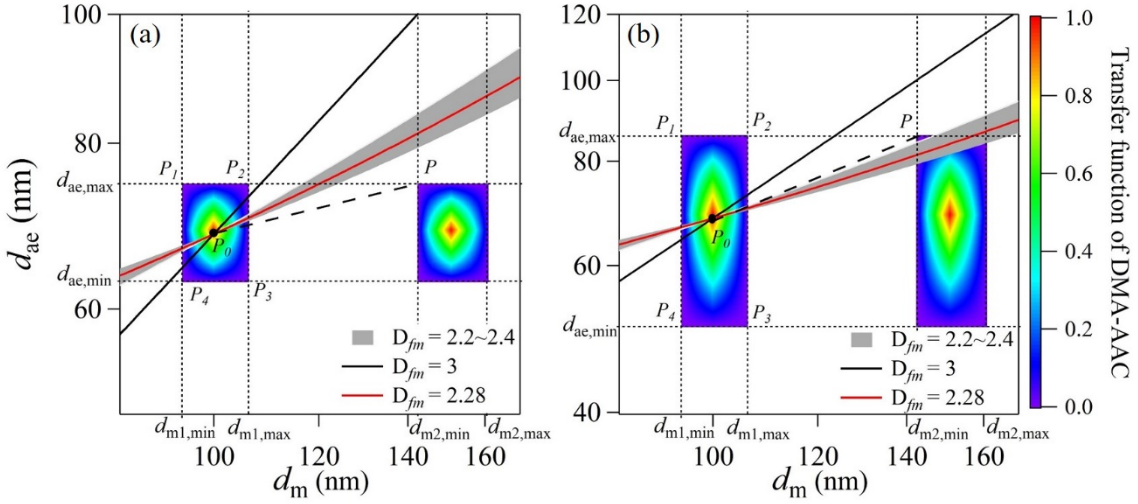

Figure 4: Examples of transfer function calculation of DMA-AAC of flame-generated soot particles (Pei et al., 2018). The following parameter set was employed for the calculations: Q_a=0.3 L min^{-1}, d_{m1} = 100 nm, d_{ae} = 68.3 nm, (a) β_{DMA} = 0.1, β_{AAC} = 0.1, (b) β_{DMA} = 0.1, β_{AAC} = 0.3. The color blocks are the transfer functions of DMA-AAC. The black and red solid lines are particle populations with D_{fm} values of 3 and 2.28, respectively. The gray region is the particles population with D_{fm} of 2.2-2.4, which is typical for soot aerosol. The dashed line is the critical slope of PP_0. The dotted lines are the limiting d_m and d_{ae} of DMA and AAC.

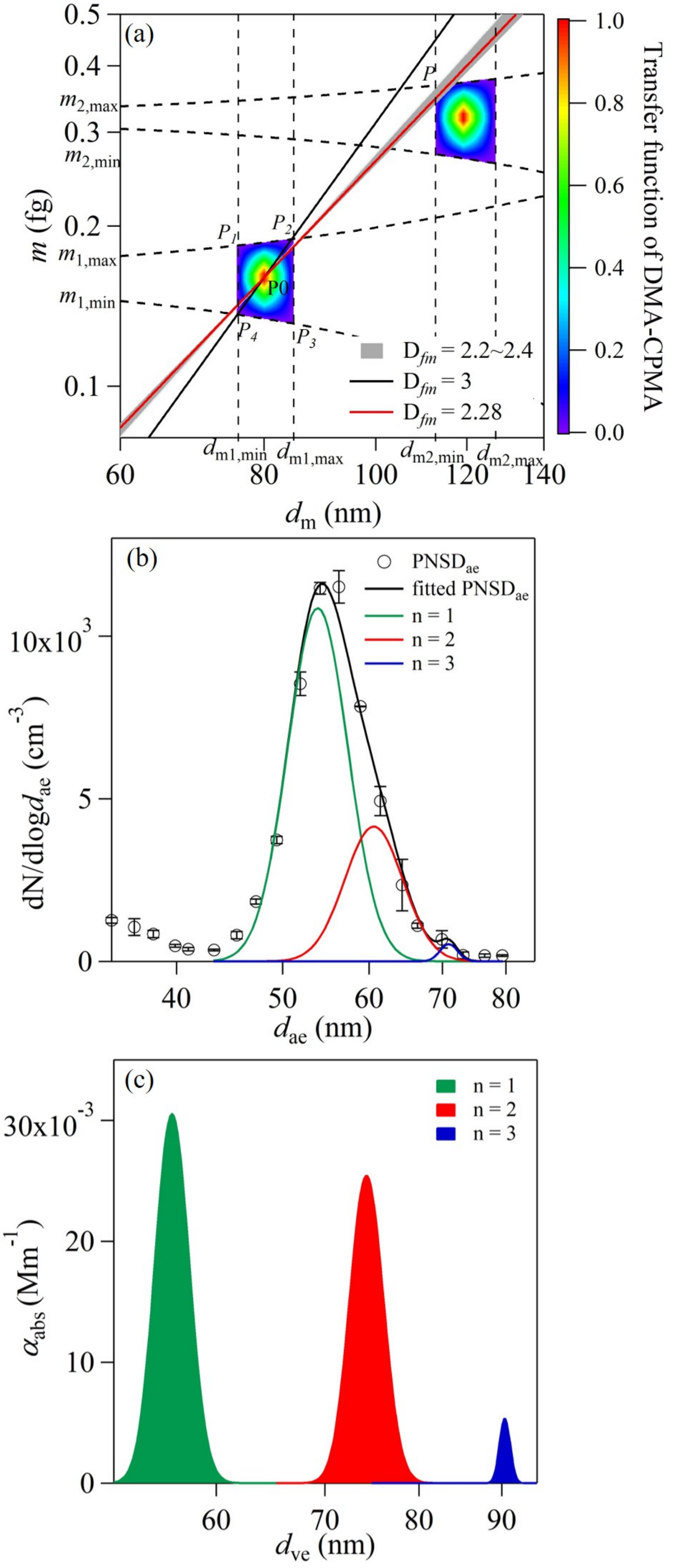
(a)
0.5
0.4
0.3
0.2
0.1
$m_{2,\mathrm{max}}$
$m_{2,\mathrm{min}}$
$m_{1,\mathrm{max}}$
$m_{1,\mathrm{min}}$
m (fg)
P
P_1
P_2
P0
P_4
P_3
D_{fm} = 2.2~2.4
D_{fm} = 3
D_{fm} = 2.28
$d_{\mathrm{m1,min}}$
$d_{\mathrm{m1,max}}$
$d_{\mathrm{m2,min}}$
$d_{\mathrm{m2,max}}$
60
80
100
120
140
d_m (nm)
1.0
0.8
0.6
0.4
0.2
0.0
Transfer function of DMA-CPMA
(b)
$\mathrm{PNSD_{ae}}$
fitted $\mathrm{PNSD_{ae}}$
n = 1
n = 2
n = 3
$10\mathrm{x}10^3$
5
0
dN/dlogd_ae ($\mathrm{cm^{-3}}$)
40
50
60
70
80
d_ae (nm)
(c)
n = 1
n = 2
n = 3
$30\mathrm{x}10^{-3}$
20
10
0
α_abs ($\mathrm{Mm^{-1}}$)
60
70
80
90
d_ve (nm)

Figure 5: (a) Transfer functions of DMA-CPMA when selecting 80 nm and 0.16 fg particles. The following parameter set was employed for the calculations: d_{m1} = 80 nm, β_{DMA} = 0.1, m_1 = 0.16 fg, Q_{CPMA}=0.3 L min^{-1}, R_m = 8. The red solid line is the generated soot particle population. (b) The aerodynamic size distribution of particles classified by DMA-CPMA. The circles are data measured by AAC-CPC, and the black, green, red and blue lines are log-normal fitted distributions of bulk, singly charged, doubly charged and triply charged particles populations. (c) The contributions to light absorption of particles with single, double and triple charges calculated with Mie theory.

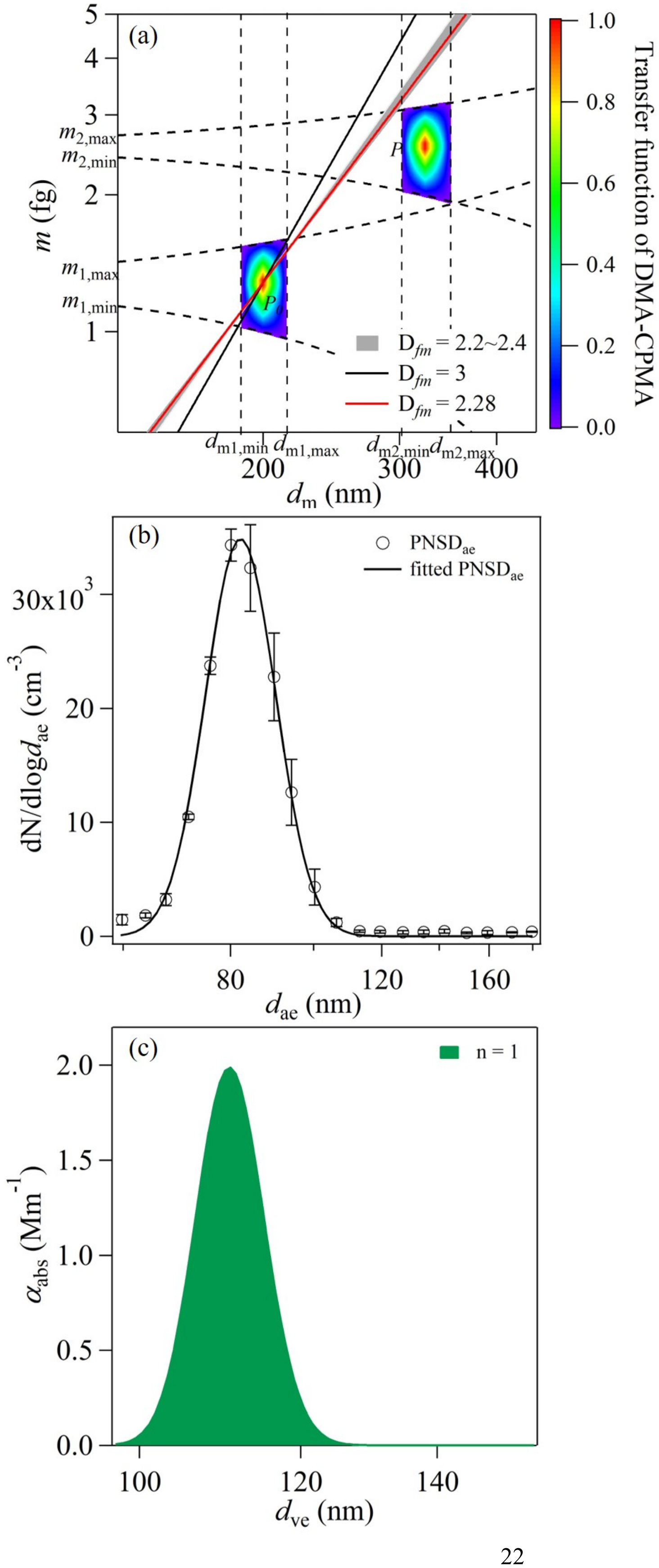
(a)
5
4
3
2
1
m (fg)
$m_{2,\max}$
$m_{2,\min}$
$m_{1,\max}$
$m_{1,\min}$
P
P
D_{fm} = 2.2~2.4
D_{fm} = 3
D_{fm} = 2.28
$d_{m1,\min}$
$d_{m1,\max}$
$d_{m2,\min}$
$d_{m2,\max}$
200
300
400
d_m (nm)
Transfer function of DMA-CPMA
1.0
0.8
0.6
0.4
0.2
0.0
(b)
PNSD$_{ae}$
fitted PNSD$_{ae}$
30x10^3
20
10
0
dN/dlogd_{ae} (cm^{-3})
80
120
160
d_{ae} (nm)
(c)
n = 1
2.0
1.5
1.0
0.5
0.0
α_{abs} (Mm^{-1})
100
120
140
d_{ve} (nm)

558

Figure 6: (a) The transfer functions of DMA-CPMA when selecting 200 nm and 1.28 fg particles. The following parameter set was employed for the calculations: d_{m1} = 200 nm, β_{DMA} = 0.1, m_1 = 1.28 fg, Q_{CPMA}=0.3 L min^{-1}, R_m = 8. The red solid line is the generated soot particle population. (b) The aerodynamic size distribution of particles classified by DMA-CPMA. The circles are data measured by AAC-CPC, and the solid line is the log-normal fitted distribution. (c) Contributions to light absorption of particles with a single charge calculated with Mie theory.